

Highly permeable artificial water channels that can self-assemble into two-dimensional arrays

Yue-xiao Shen^a, Wen Si^b, Mustafa Erbakan^a, Karl Decker^c, Rita De Zorzi^{d,e}, Patrick O. Saboe^a, You Jung Kang^f, Sheereen Majd^f, Peter J. Butler^f, Thomas Walz^{d,e}, Aleksei Aksimentiev^c, Jun-li Hou^b, and Manish Kumar^{a,1}

^aDepartment of Chemical Engineering, The Pennsylvania State University, University Park, PA 16802; ^bDepartment of Chemistry, Fudan University, Shanghai 200433, China; ^cDepartment of Physics, University of Illinois at Urbana-Champaign, Urbana, IL 61801; ^dDepartment of Cell Biology, Harvard Medical School, Boston, MA 02115; ^eHoward Hughes Medical Institute, Harvard Medical School, Boston, MA 02115; and ^fDepartment of Biomedical Engineering, The Pennsylvania State University, University Park, PA 16802

Approved July 7, 2015

Bioinspired artificial water channels aim to combine the high permeability and selectivity of biological aquaporin (AQP) water channels with chemical stability. Here, we carefully characterized a class of artificial water channels, peptide-appended pillar[5]arenes (PAPs). The average single-channel osmotic water permeability for PAPs is $1.0(\pm 0.3) \times 10^{-14}$ cm³/s or $3.5(\pm 1.0) \times 10^8$ water molecules per s, which is in the range of AQPs ($3.4\sim 40.3 \times 10^8$ water molecules per s) and their current synthetic analogs, carbon nanotubes (CNTs, 9.0×10^8 water molecules per s). This permeability is an order of magnitude higher than first-generation artificial water channels (20 to $\sim 10^7$ water molecules per s). Furthermore, within lipid bilayers, PAP channels can self-assemble into 2D arrays. Relevant to permeable membrane design, the pore density of PAP channel arrays ($\sim 2.6 \times 10^5$ pores per μm^2) is two orders of magnitude higher than that of CNT membranes ($0.1\sim 2.5 \times 10^3$ pores per μm^2). PAP channels thus combine the advantages of biological channels and CNTs and improve upon them through their relatively simple synthesis, chemical stability, and propensity to form arrays.

artificial aquaporins | artificial water channels | peptide-appended pillar[5]arene | single-channel water permeability | two-dimensional arrays

The discovery of the high water and gas permeability of aquaporins (AQPs) and the development of artificial analogs, carbon nanotubes (CNTs), have led to an explosion in studies aimed at incorporating such channels into materials and devices for applications that use their unique transport properties (1–9). Areas of application include liquid and gas separations (10–13), drug delivery and screening (14), DNA recognition (15), and sensors (16). CNTs are promising channels because they conduct water and gas three to four orders of magnitude faster than predicted by conventional Hagen–Poiseuille flow theory (11). However, their use in large-scale applications has been hampered by difficulties in producing CNTs with subnanometer pore diameters and fabricating membranes in which the CNTs are vertically aligned (4). AQPs also efficiently conduct water across membranes (~ 3 billion molecules per second) (17) and are therefore being studied intensively for their use in biomimetic membranes for water purification and other applications (1, 2, 18). The large-scale applications of AQPs is complicated by the high cost of membrane protein production, their low stability, and challenges in membrane fabrication (1).

Artificial water channels, bioinspired analogs of AQPs created using synthetic chemistry (19), ideally have a structure that forms a water-permeable channel in the center and an outer surface that is compatible with a lipid membrane environment (1). Interest in artificial water channels has grown in recent years, following decades of research and focus on synthetic ion channels (19). However, two fundamental questions remain: (i) Can artificial channels approach the permeability and selectivity of AQP water channels? (ii) How can such artificial channels be packaged into materials with morphologies suitable for engineering applications?

Because of the challenges in accurately replicating the functional elements of channel proteins, the water permeability and selectivity of first-generation artificial water channels were far below those of AQPs (*SI Appendix, Table S1*) (20–25). In some cases, the conduction rate for water was much lower than that of AQPs as a result of excess hydrogen bonds being formed between the water molecules and oxygen atoms lining the channel (20). The low water permeability that was measured for first-generation water channels also highlights the experimental challenge of accurately characterizing water flow through low-permeability water channels. Traditionally, a liposome-based technique has been used to measure water conduction, in which the response to an osmotic gradient is followed by measuring changes in light scattering (26, 27) or fluorescence (28). The measured rates are then converted to permeability values. These measurements suffer from a high background signal due to water diffusion through the lipid bilayer, which, in some cases, can be higher than water conduction through the inserted channels, making it challenging to resolve the permeability contributed by the channels (29). Thus, there is a critical need for a method to accurately measure single-channel permeability of artificial water channels to allow for accurate comparison with those of biological water channels. Furthermore, first-generation artificial water channels were designed with a focus on demonstrating water conduction and one-dimensional assembly into tubular structures (20–24), but how the channels could be assembled

Significance

This study focuses on the design of highly permeable artificial water channels for the use in membrane-based separation materials. A platform was developed for the systematic characterization of the single-channel water conduction of artificial channels, which is based on permeability measurement by stopped-flow light-scattering experiments and single-molecule counting by fluorescence correlation spectroscopy. With this platform the water conduction of the redesigned peptide-appended pillar[5]arene channels was found to be similar to that of aquaporins, natural water channel proteins, and their synthetic analogs, carbon nanotubes, which is an order of magnitude higher than that of first-generation artificial water channels. The channel can also self-assemble into arrays in membranes, opening the possibility for materials that can be used in engineering applications such as liquid and gas separations.

Author contributions: Y.-x.S., S.M., P.J.B., T.W., A.A., J.-I.H., and M.K. designed research; Y.-x.S., W.S., M.E., K.D., R.D.Z., P.O.S., and Y.J.K. performed research; S.M., P.J.B., T.W., A.A., and J.-I.H. contributed new reagents/analytic tools; Y.-x.S., W.S., M.E., K.D., R.D.Z., P.O.S., Y.J.K., S.M., P.J.B., T.W., A.A., J.-I.H., and M.K. analyzed data; and Y.-x.S., T.W., A.A., and M.K. wrote the paper.

The authors declare no conflict of interest.

¹To whom correspondence should be addressed. Email: manish.kumar@psu.edu.

into materials suitable for use in engineering applications was not explored. To derive the most advantage from their fast and selective transport properties, artificial water channels are ideally vertically aligned and densely packed in a flat membrane. These features have been long desired but remain a challenge for CNT-based systems (4).

Here we introduce peptide-appended pillar[5]arene (PAP; Fig. 1) (30) as an excellent architecture for artificial water channels, and we present data for their single-channel permeability and self-assembly properties. Nonpeptide pillar[5]arene derivatives were among first-generation artificial water channels (1, 23). Pillar[5]arene derivatives, including the one used in this study, have a pore of ~ 5 Å in diameter and are excellent templates for functionalization into tubular structures (31–34). However, the permeability of hydrazide-appended pillar[5]arene channels was low (~ 6 orders of magnitude lower than that of AQPs; *SI Appendix, Table S1*). We addressed the challenges of accurately measuring single-channel water permeability and improving the water conduction rate over first-generation artificial water channels by using both experimental and simulation approaches. The presented PAP channel contains more hydrophobic regions (30) compared with its predecessor channel (23), which improves both its water permeability and its ability to insert into membranes. To determine single-channel permeability of PAPs, we combined stopped-flow light-scattering measurements of lipid vesicles containing PAPs with fluorescence correlation spectroscopy (FCS) (35, 36). Stopped-flow experiments allow the kinetics of vesicle swelling or shrinking to be followed with millisecond resolution and water permeability to be calculated, whereas FCS makes it possible to count the number of channels per vesicle (36, 37). The combination of the two techniques allows molecular characterization of channel properties with high resolution and demonstrates that PAP channels have a water permeability close to those of AQPs and CNTs. The experimental results were corroborated by molecular dynamics (MD) simulations, which also provided additional insights into orientation and aggregation of the channels in lipid membranes. Finally, as a first step toward engineering applications such as liquid and gas separations, we were able to assemble PAP channels into highly packed planar membranes, and we experimentally confirmed that the channels form 2D arrays in these membranes.

Single-Channel Water Permeability

The PAP channel was functional in phosphatidylcholine/phosphatidylserine (PC/PS) liposomes, but its water conduction rates differed under hypertonic and hypotonic conditions (Fig. 2). We first considered the permeability under hypertonic conditions. Upon establishing outwardly directed osmotic gradients, the liposomes shrank, and the light-scattering signal at 90° increased. The curves could be fit in the form of a sum of two exponential functions, indicating two shrinkage rates, one characterized by a

large exponential constant, k_1 , that was independent of the density of channels in the vesicles and the other one characterized by a smaller constant, k_2 , that increased with increasing molar channel-to-lipid ratios (mCLRs) (Fig. 2A). This result indicated that the contribution of the PAP channels to the overall water permeability of the vesicles was lower than that of the lipid membrane, and so the smaller exponential coefficient (k_2) was used to calculate the permeability of the channel. The same approach was recently used to measure the low water permeability of AQP0 (38). The permeability contributed by the PAP channels increased linearly when the mCLR was increased from 0 to 0.005 (Fig. 2B). In contrast, when vesicles with reconstituted PAP channels were exposed to hypotonic solutions (under these conditions the vesicles swelled and the light scattering signal measured at 90° decreased), there was a significant increase in the larger exponential constant (k_1) over that of the control vesicles (Fig. 2C). The net permeability calculated in the swelling mode was found to be 61 times higher than that in the shrinking mode (Fig. 2D). Water conduction by PAP channels was further confirmed by a set of experiments on giant unilamellar vesicles (*SI Appendix, Figs. S1 and S2*), showing that vesicles containing PAP channels swell significantly faster than pure lipid vesicles (*Movie S1*). The effect of residual DMSO, the solvent used for the channel, on the permeability of the vesicles was found to be negligible (*SI Appendix, Fig. S3*).

To calculate the average single-channel permeability of PAP channels, an FCS technique was used to count the number of channels per vesicle (36, 37). The channels were tagged with a fluorophore, tetramethylrhodamine cadaverine, using dicyclohexylcarbodiimide as the crosslinking reagent (Fig. 2E). The labeling process was optimized to ensure that all channels were labeled (*SI Appendix, Figs. S4–S6*), and the labeled channels were incorporated into PC/PS liposomes. A two-species model was used to fit the auto-correlation curves of both liposomes and micelles to differentiate them from free fluorophores. Curve fitting yielded the number of fluorescent liposomes ($N_{\text{Liposomes}}$) (the inverse of the correlation function amplitude) in the confocal volume. The liposomes were then solubilized in 2.5% (wt/vol) octyl glucoside (OG) to release the labeled channels into micelles (Fig. 2E), and the number of the micelles (N_{Micelles}) was obtained by fitting.

As expected, the diffusion time (τ_d) for labeled channels in liposomes was longer than those for channels in detergent micelles (Fig. 2F). The size of detergent micelles with and without channels, as determined by both FCS and dynamic light scattering, was similar, which implies that most micelles contain only one channel molecule (Fig. 2F and *SI Appendix, Table S2*). The subsequently calculated insertion efficiency (*SI Appendix, Fig. S7*) shows that if micelles contained two or three channels, the insertion efficiency would be better than 100%, which is not possible. With these insertion efficiency considerations, together with size measurements and the amount of detergent used during

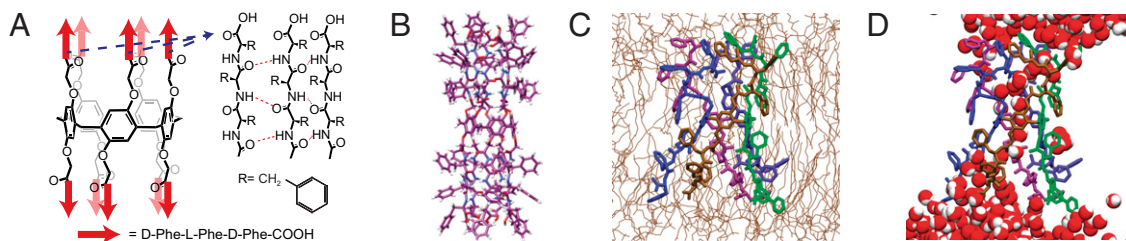


Fig. 1. Structure of the peptide-appended pillar[5]arene (PAP) channel. (A) The PAP channel ($C_{325}H_{320}N_{30}O_{60}$) forms a pentameric tubular structure through intramolecular hydrogen bonding between adjacent alternating D-L-D phenylalanine chains (D-Phe-L-Phe-D-Phe-COOH). (B) Molecular modeling (Gaussian09, semiempirical, PM6) of the PAP channel shows that the benzyl rings of the phenylalanine side chains extend outward from the channel walls (C, purple; H, white; O, red; N, blue). (C and D) MD simulation of the PAP channel in a POPC bilayer revealed its interactions with the surrounding lipids. The five chain-like units of the channel are colored purple, blue, ochre, green, and violet, with hydrogen atoms omitted. In C, the POPC lipids are represented by thin tan lines; in D, water is shown as red (oxygen) and white (hydrogen) van der Waals spheres.

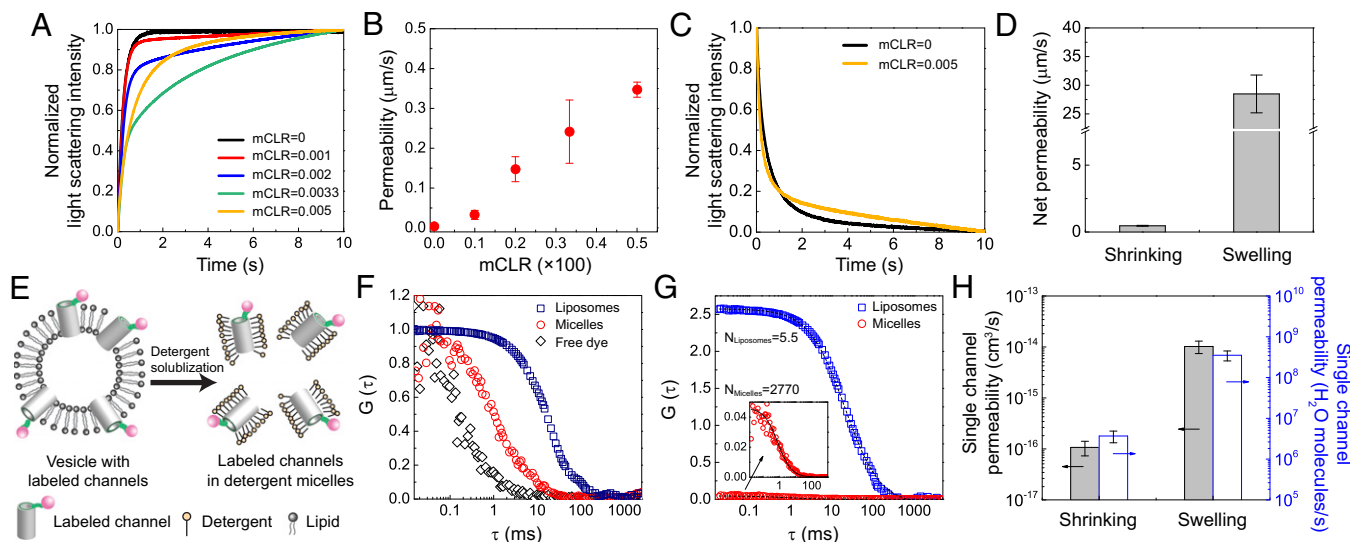


Fig. 2. The water permeability of PAP channels was calculated using a combination of stopped-flow and fluorescence correlation spectroscopy (FCS) experiments. (A) Representative stopped-flow traces from experiments performed on liposomes formed with different molar channel-to-lipid ratios (mCLRs; 0, 0.001, 0.002, 0.0033, and 0.005) after a rapid exposure to a hypertonic solution containing 400 mM sucrose. (B) The water permeability of PAP channel-containing liposomes formed with different mCLRs measured under hypertonic conditions. Data shown are the average of triplicates with error bars representing standard deviation (SD). (C) Representative stopped-flow traces from experiments performed on liposomes with mCLRs of 0 and 0.005 after rapid exposure to a buffer without the 100 mM PEG600 used to form the vesicles. (D) Net channel permeability measured for PAP channel-containing liposomes (mCLR = 0.005) under vesicle shrinking and swelling conditions. (E) FCS was used to determine the number of PAP channels per vesicle. First, FCS was used to analyze vesicles containing fluorescently labeled channels (Left). The vesicles were then solubilized with detergent, releasing the channels into detergent micelles (Right), and the solution was again analyzed by FCS. (F) The normalized FCS autocorrelation curves of the free dye tetramethylrhodamine cadaverine, labeled PAP channel in detergent micelle, and vesicles incorporating the labeled PAP channel. They have significantly different diffusion coefficients [D_x represents diffusion coefficient of x species, whereas d_x represents the estimated diameter, $D_{\text{free dye}} = 4.6(\pm 0.6) \times 10^{-6} \text{ cm}^2/\text{s}$, $d_{\text{free dye}} = 1.0 \pm 0.1 \text{ nm}$; $D_{\text{Micelles}} = 5.3(\pm 0.2) \times 10^{-7} \text{ cm}^2/\text{s}$, $d_{\text{Micelles}} = 8.5 \pm 0.4 \text{ nm}$; $D_{\text{Liposomes}} = 2.4(\pm 0.2) \times 10^{-8} \text{ cm}^2/\text{s}$, $d_{\text{Liposomes}} = 191.3 \pm 18.2 \text{ nm}$]. The FCS measurements give a diameter of the micelles containing PAP channel of $8.5 \pm 0.4 \text{ nm}$, close to the value determined by dynamic light scattering (DLS) ($8.4 \pm 0.1 \text{ nm}$). The channel-containing micelles were slightly larger than pure OG micelles ($7.8 \pm 0.2 \text{ nm}$, determined by DLS), indicating that each micelle contains only a single channel. (G) The FCS autocorrelation curves for vesicles with labeled PAP channels (mCLR = 0.005) before and after solubilization with 2.5% (wt/vol) OG. The high correlation function amplitude $G(0)$ obtained for the vesicles indicates a low number of fluorescent liposomes in the confocal volume ($N_{\text{Liposomes}}$). After detergent solubilization, the number of free particles increased by more than 500 times (N_{Micelles}). The number of channels per vesicle was then calculated as $N_{\text{Micelles}}/N_{\text{Liposomes}}$. (H) Single-channel water permeability of the PAP channel (obtained from the vesicles formed at an mCLR of 0.005; permeability data are from D). Data shown are the average of triplicates with error bars representing SD.

FCS experiments, it is most likely that most micelles contained only one channel. However, even if some micelles contained two channels per micelle, the experimentally determined single-channel permeability values would only drop by a factor of two, not affecting the order of magnitude of the determined permeability.

The lower correlation amplitude indicated that solubilization created a large number of fluorescent micelles (Fig. 2G). The number of the labeled channels per liposome (N_{Channels}) was calculated as the ratio $N_{\text{Micelles}}/N_{\text{Liposomes}}$. Compared with the theoretical number of channels that could be inserted into a liposome of $\sim 150 \text{ nm}$ in diameter, the size used in our experiments, the calculated number corresponded to an insertion efficiency of $\sim 45\%$ (SI Appendix, Fig. S7). Because fluorophore labeling reduced the water conductance of PAP channels in the shrinking mode (SI Appendix, Fig. S8), single-channel permeability (Fig. 2H) was calculated using the number of channels determined by FCS and the permeability data obtained with unlabeled channels for both modes (Fig. 2D). In the shrinking mode, the PAP channel has a water permeability of $1.1(\pm 0.3) \times 10^{-16} \text{ cm}^3/\text{s}$, corresponding to $3.7(\pm 1.2) \times 10^6$ water molecules per s. In the swelling mode, the water conduction of the channel is ~ 2 orders of magnitude higher than that in the shrinking mode, with a measured permeability of $1.0(\pm 0.3) \times 10^{-14} \text{ cm}^3/\text{s}$, corresponding to $3.5(\pm 1.0) \times 10^8$ water molecules per s.

MD Simulations

MD calculations (39) were performed with a system of 25 regularly spaced PAP channels in a 1-palmitoyl-2-oleoyl-*sn*-glycero-

3-phosphatidylcholine (POPC) bilayer that was surrounded by water molecules (Fig. 3A). The simulations revealed several interesting features. First, individual channels exhibited wetting-dewetting transitions, i.e., the average fraction of channels filled with water fluctuated over the simulation time (Fig. 3B and Movie S2). After 30 ns of unrestrained simulation, on average, 40% of the channels were filled with water, regardless of whether simulations were initiated with water-filled or empty PAP channels. Fig. 3C illustrates the occupancy of a typical PAP channel over a 150-ns segment of a MD trajectory, showing that it takes less than 3 ns for a channel to transition from completely wet to completely dry. The water occupancy probability of a single channel (Fig. 3C, Inset) averaged over all microscopic states observed in our MD simulations has two maxima, corresponding to the dry and wet states. The snapshots in Fig. 3D illustrate the microscopic conformation of the channel before and after the wetting-dewetting transitions. Such transitions have also been observed in other biological and artificial channel systems (40–42). Second, the PAP channels had a propensity to aggregate into clusters (Fig. 3E). For example, in the 240-ns simulation initiated with water-filled channels, the average number of channels being part of a cluster increased from 1 to 13 (Movie S3). Visual inspection identified hydrogen bonds between the carboxyl and amine groups at the peptide chains of the neighboring channels stabilized the aggregates. Third, the channels showed considerable dynamics in the lipid bilayer. Although the peptide side chains remained rigid in the

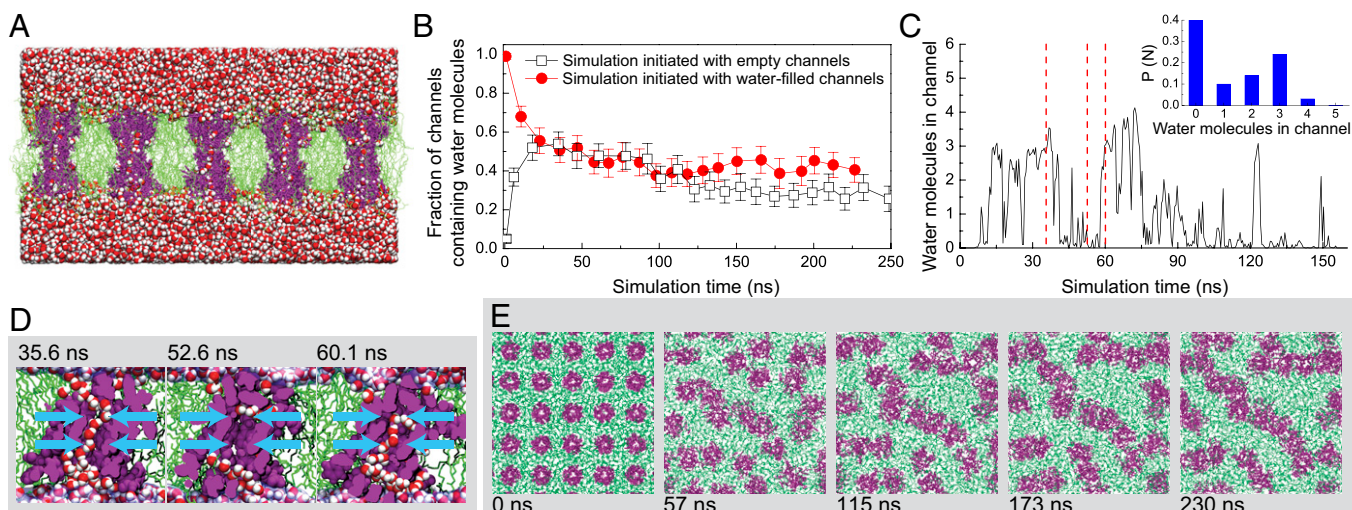


Fig. 3. MD simulations of PAP channels in a lipid environment reveal wetting–dewetting transitions of the pore and a tendency of the channels to aggregate. (A) A cutaway view of the simulated system. PAP channels are depicted in purple, the POPC bilayer is in green, and water molecules are shown as red and white van der Waals spheres. The image shows the system 1 ns after inserting water molecules into the channels. (B) The average fraction of channels that contain water molecules as a function of the simulation time. Irrespective of whether the simulations were initiated with empty or water-filled channels, the system equilibrated to ~40% of the channels containing water. In this plot, 0 ns corresponds to the beginning of free equilibration. The error bars represent the error of the mean. (C) The number of water molecules present in a PAP channel during a representative fragment of an MD trajectory. *Inset* shows the normalized probability of observing a given number of water molecules in a PAP channel. The probability was computed by examining the occupancy of all channels during the last 200 ns of two MD trajectories sampled every 0.1 ns. Red dashed lines indicate the time points of the snapshots shown in D. (D) Wetting/dewetting of a PAP channel. The channel is shown as purple van der Waals spheres, POPC lipids are shown in green stick representation, and water molecules are shown by red and white van der Waals spheres. The cyan arrows indicate the region of the channel that was used to determine the occupancy and permeability of the channels. (E) A sequence of snapshots illustrating the aggregation of PAP channels in the lipid bilayer. Each image shows a top view of the simulation system. PAP channels are depicted in purple, POPC lipids are shown in green stick representation, and water is not shown. When released from constraints, channels migrate through the membrane and form clusters. For the simulations initiated with water-filled channels, the average cluster sizes with SD were as follows: 0 ns, 1.0 ± 0.0 ; 57 ns, 1.9 ± 1.4 ; 115 ns, 3 ± 3 ; 173 ns, 8 ± 6 ; and 230 ns, 13 ± 13 . Simulations initiated with empty channels showed similar clustering behavior.

Gaussian model due to interchain hydrogen bonds (Fig. 1 A and B), the side chains exhibited greater flexibility as they interacted with the hydrophobic core of the lipid bilayer (Movie S4). In addition, the PAP channels tended to be tilted with respect to the membrane plane, and although the angle varied considerably from channel to channel (SI Appendix, Fig. S9), the most probable angle was 25° . A few channels were observed to tilt so much that they no longer spanned the membrane.

The water permeability was calculated using a collective diffusion model for a system in equilibrium (43). To test its appropriateness, the method was first used to calculate the permeability of AQP1. The calculated value of $2.0(\pm 0.1) \times 10^{-13} \text{ cm}^3/\text{s}$ was within the range of previously determined values ($1.4\text{--}2.9 \times 10^{-13} \text{ cm}^3/\text{s}$) (44). For simulations on PAP channels, the root mean square deviation (RMSD) of the coordinates of the channels with respect to their crystallographic coordinates (SI Appendix, Fig. S10) and the fraction of water-filled channels (Fig. 3B) showed that the system had converged to equilibrium after 30 ns. Hence, MD trajectory data from that time onward were used to calculate the water permeability. Simulations yielded a very similar average permeability irrespective of whether simulations were initiated with water-filled or empty channels, $1.9(\pm 0.4) \times 10^{-14} \text{ cm}^3/\text{s}$ and $1.5(\pm 0.5) \times 10^{-14} \text{ cm}^3/\text{s}$, respectively. Individual channels exhibited considerable variability with permeability values ranging from 0.1 to $3.1 \times 10^{-14} \text{ cm}^3/\text{s}$ within the 240-ns simulation. The average tilt of a channel showed little correlation with its water permeability provided the channel remained accessible to water from both sides of the membrane. Of the 50 simulated channels, about 10 channels showed low water conductance ($<3 \times 10^{-15} \text{ cm}^3/\text{s}$) at any given moment of the MD simulations. At any time during the simulation, on average, approximately nine of these ten were devoid of water, and

seven of these ten had the entrance blocked by a phenylalanine chain. For one low-conductance channel, one acyl chain of a lipid molecule entered the channel, blocking it completely for the remainder (>200 ns) of the simulation (Movie S5 and SI Appendix, Fig. S11). We speculate that an increase in the fraction of low-conductance channels in the shrinking mode by one of the mechanisms described above might reduce osmotic permeability compared with that under the swelling mode. However, simulations for the shrinking mode, in which the area occupied by channels and lipids was reduced, did not reveal an increase in the number of low-conductance channels. Longer and more detailed simulations will be required to investigate this effect.

Self-Assembly Behavior

Pillar[5]arene channels can be packed into lipid membranes with very high densities. A slow dialysis technique (45) was used to conduct self-assembly experiments with PAP channels and lipids over a wide range of mCLR. Like for membrane proteins (46), the concentration of PAP channels in the membrane had a significant effect on the morphology of the resulting PAP channel–lipid aggregates as observed by negative-stain electron microscopy (EM) (Fig. 4A). When the channel concentration was low (below an mCLR of 0.05), dialysis produced vesicles mostly with a diameter of 100–200 nm. When the mCLR was increased to ~0.5, the vesicles grew to approximately 1 μm in diameter. At mCLR of 0.714, sheet-like membranes began to form. At mCLR higher than 1, channel aggregates were observed in addition to membrane-like morphologies (see SI Appendix, Fig. S12, for the different aggregate morphologies observed over the full mCLR range). Increasing the density of the channel in the membrane thus changed the curvature of the lipid bilayer and resulted in the formation of flat membranes. The mCLR at

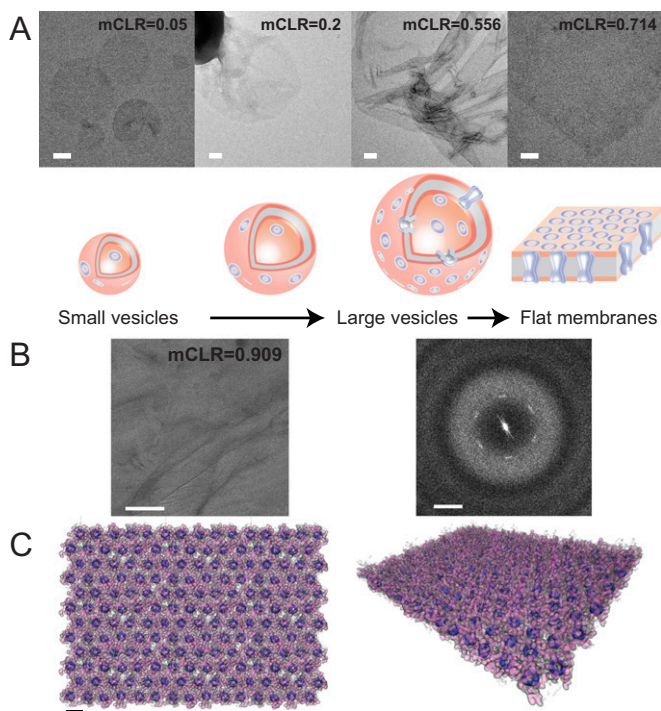


Fig. 4. The concentration of PAP channels influences the morphology of self-assembled channel-lipid aggregates. (A) Negative-stain EM images show the representative morphologies of aggregates formed at different molar channel-to-lipid ratios (mCLRs). Increasing mCLRs from 0.05 to 0.2 to 0.625 to 0.714 resulted in morphology transitions from small vesicles to large vesicles and finally to flat membranes. Scale bars are 100 nm. (B) (Left) A cryo-EM image of a self-assembled channel-lipid aggregate formed at an mCLR of 0.909 that was frozen in trehalose. (Scale bar, 100 nm.) (Right) The power spectrum, which reveals blurry first-order diffraction spots, indicating that the PAP channels form a somewhat ordered hexagonal array with lattice dimensions of $a = b = 21 \text{ \AA}$ and $\gamma = 120^\circ$. (Scale bar, 0.5 nm^{-1} .) (C) Top (Left) and tilted (Right) views of a molecular model of a partially ordered array of hexagonally packed PAP channels in a lipid bilayer. The inner channel rings (dimethoxy benzene) are rendered as opaque dark violet surfaces, phenylalanine arms are rendered as translucent purple surfaces, and lipid molecules are rendered as transparent gray polygons. For clarity, water is not shown. The model is the result of an MD simulation guided by the ordering observed in the cryo-EM images. (Scale bar, 2.1 nm.)

which the PAP channel-lipid aggregates transition from curved to flat membranes was close to 0.5, compared with a range of 0.02–0.125 for most membrane protein-lipid aggregates (45). The transition at a lower mCLR for PAP channel-lipid aggregates can be explained by the cross-sectional area of the PAP channel, which is smaller than that of most membrane proteins. To further analyze the packing of the channels in the membranes, PAP channel-containing vesicles produced at an mCLR of 0.909 were prepared by the carbon sandwich technique (47) and analyzed by cryo-EM (Fig. 4B, Left). Power spectra of the images showed blurry first-order diffraction spots, indicating the presence of very densely packed or even somewhat ordered regions with lattice constants of $a = b = 21 \text{ \AA}$ and $\gamma = 120^\circ$ (Fig. 4B, Right). Considering that the entire cross-sectional area of the channel is $\sim 300 \text{ \AA}^2$, a single unit cell within the 2D crystal can only accommodate one channel molecule. The PAP channels are most likely densely packed in a hexagonal arrangement. A molecular model of these densely packed PAP sheets is shown in Fig. 4C.

Solute Rejection and Ion Selectivity

Stopped-flow light-scattering measurements were also performed in the presence of osmolytes of different molecular weights (*SI*

Appendix, Figs. S13–S15). The reflection coefficient for each osmolyte was calculated as the ratio of the measured water permeability in its presence to that in the presence of a completely retained osmolyte (Dextran500) (48). Based on a reflection coefficient of 0.9, the molecular weight cutoff of the PAP channel was determined to be $\sim 420 \text{ Da}$ (*SI Appendix*, Fig. S16), consistent with its pore diameter of $\sim 5 \text{ \AA}$. The ion selectivity of the channel was determined by patch-clamp experiments. The voltage-current relationship showed PAP channels to be cation selective (*SI Appendix*, Fig. S17), which was expected as the channel has five carboxylic groups at each entrance. The order of ion selectivity was $\text{NH}_4^+ > \text{Cs}^+ > \text{Rb}^+ > \text{K}^+ > \text{Na}^+ > \text{Li}^+ > \text{Cl}^-$ (*SI Appendix*, Table S3).

Comparison of PAP Channels with AQPs and CNTs

The water permeability of the PAP channel under swelling conditions is only one order of magnitude lower than that of AQP1, the AQP with the highest water permeability ($11.7 \times 10^{-14} \text{ cm}^3/\text{s}$) (49), and is close to that of CNTs ($2.61 \times 10^{-14} \text{ cm}^3/\text{s}$) (12). If water channels are to be used in separation materials, it is important to consider their effective cross-sectional area. AQPs occupy a large cross-sectional area in the membrane ($\sim 9 \text{ nm}^2$), but the actual water pore represents only a very small portion of the occupied membrane area (*SI Appendix*, Fig. S18). This will offset the high water permeability of AQPs, even if a membrane is very densely packed with AQPs, such as in 2D crystals (1, 45). Taking into account the cross-sectional areas of the PAP channel (3.0 nm^2), AQP1 (9.0 nm^2) (50), and CNTs (2.1 nm^2) (12, 51), the single-channel permeability of the PAP channel per cross-sectional area is similar to that of the most water-permeable AQPs and CNTs (*SI Appendix*, Fig. S18). Artificial water channels provide two additional advantages over channel proteins, namely, high physicochemical stability as well as solubility in and compatibility with organic solvents. The latter is particularly critical for membrane fabrication because organic solvents are used in polymer membrane processing. A method based on solvent casting to self-assemble artificial water channels in lamellar amphiphilic block copolymers may allow scalable manufacturing of high-permeability membranes.

PAP channels also present advantages over CNTs. First, the structure of the PAP channel could be further modified so that the pore size is compatible for use in water desalination. The majority of currently reported artificial water channels have a pore diameter of less than 0.6 nm (*SI Appendix*, Table S1), but CNTs with this pore size cannot yet be synthesized (4). Furthermore, artificial channels with specially designed pore sizes may not only be useful in water purification but also hold promise in other fields currently proposed for CNT-based systems, such as biomolecule sensing, gas separations, drug delivery, and protective fabrics (4–6, 15, 52). Second, most CNTs produced in bulk today suffer from disorganized architectures (4), which significantly limit their use in applications that depend on transport through their pores. The experimental and simulation studies presented here demonstrate that the PAP channels are aligned in lipid bilayers, and that PAP channels can form 2D arrays, mimicking crystalline protein arrays found in some biological membranes, such as the mammalian eye fiber cell membranes (53), retinal rod membranes (54), and photosynthetic membranes (55). The packing density of the PAP channels ($2.6 \times 10^7/\mu\text{m}^2$) is higher than those of AQP 2D crystals ($8.6 \times 10^4/\mu\text{m}^2$ for AQP1 and $9.5 \times 10^4/\mu\text{m}^2$ for AQP0) (56, 57) and two orders of magnitude higher than those of current CNT-based membranes ($0.1 \sim 2.5 \times 10^7/\mu\text{m}^2$) (12, 58–61) (*SI Appendix*, Table S4). Taking into account the effective cross-sectional pore areas of the membranes, the packing of PAP channels at an mCLR close to 0.5 is also far more efficient than that of cyclic peptide nanotubes in block copolymer membranes (62). Third, pillar[n]arene-based artificial channels present the opportunity for simple modifications of their

side chains to change their transport properties. Compared with hydrazide-appended pillar[n]arene (23), the presented peptide-appended pillar[5]arene channels have greatly improved water permeability and membrane insertion characteristics. A drawback of the current PAP channel is its substrate selectivity. With a molecular weight cutoff of 420 Da, the channel is not suitable to remove salt and other small solutes. However, the ability to attach different substituents to the pillar[5]arene scaffold may provide a way to enhance selectivity. Overall, this study shows the promise of pillar[5]arene-based artificial water channels to mimic the high permeability of biological water channels and carbon nanotubes.

Materials and Methods

SI Appendix provides detailed materials and methods, including preparation of lipid vesicles, water permeability measurements, water permeability of giant unilamellar vesicles (GUVs), labeling procedure and estimating labeling efficiency, FCS, MD simulations, self-assembly of PAP channel/lipid aggregates and EM imaging, and solute rejection.

ACKNOWLEDGMENTS. T.W. is an investigator with the Howard Hughes Medical Institute. K.D. was supported through a cooperative research agreement with the Army Corps of Engineers Engineer Research and Development Center–Construction Engineering Research Laboratory. The authors acknowledge supercomputer time provided through Extreme Science and Engineering Discovery Environment (XSEDE) Allocation Grant MCA055028 and the Blue Waters petascale supercomputer system at the University of Illinois at Urbana-Champaign. P.J.B. was funded through a grant from the National Science Foundation (NSF CMMI 1334847).

- Shen Y-x, Saboe PO, Sines IT, Erbakan M, Kumar M (2014) Biomimetic membranes: A review. *J Membr Sci* 454:359–381.
- Nielsen C (2009) Biomimetic membranes for sensor and separation applications. *Anal Bioanal Chem* 395(3):697–718.
- Baughman RH, Zakhidov AA, de Heer WA (2002) Carbon nanotubes—The route toward applications. *Science* 297(5582):787–792.
- De Volder MFL, Tawfik SH, Baughman RH, Hart AJ (2013) Carbon nanotubes: Present and future commercial applications. *Science* 339(6119):535–539.
- Bianco A, Kostarelos K, Prato M (2005) Applications of carbon nanotubes in drug delivery. *Curr Opin Chem Biol* 9(6):674–679.
- Kauffman DR, Star A (2008) Carbon nanotube gas and vapor sensors. *Angew Chem Int Ed* 47(35):6550–6570.
- Shannon MA, et al. (2008) Science and technology for water purification in the coming decades. *Nature* 452(7185):301–310.
- Elimelech M, Phillip WA (2011) The future of seawater desalination: Energy, technology, and the environment. *Science* 333(6043):712–717.
- García-Fandiño R, Sansom MSP (2012) Designing biomimetic pores based on carbon nanotubes. *Proc Natl Acad Sci USA* 109(18):6939–6944.
- Hinds BJ, et al. (2004) Aligned multiwalled carbon nanotube membranes. *Science* 303(5654):62–65.
- Majumder M, Chopra N, Andrews R, Hinds BJ (2005) Nanoscale hydrodynamics: Enhanced flow in carbon nanotubes. *Nature* 438(7064):44.
- Holt JK, et al. (2006) Fast mass transport through sub-2-nanometer carbon nanotubes. *Science* 312(5776):1034–1037.
- Corry B (2008) Designing carbon nanotube membranes for efficient water desalination. *J Phys Chem B* 112(5):1427–1434.
- Wu J, et al. (2010) Programmable transdermal drug delivery of nicotine using carbon nanotube membranes. *Proc Natl Acad Sci USA* 107(26):11698–11702.
- Williams KA, Veenhuizen PTM, de la Torre BG, Eritja R, Dekker C (2002) Nanotechnology: Carbon nanotubes with DNA recognition. *Nature* 420(6917):761.
- Li J, et al. (2003) Carbon nanotube sensors for gas and organic vapor detection. *Nano Lett* 3(7):929–933.
- Agre P (2004) Aquaporin water channels (Nobel Lecture). *Angew Chem Int Ed* 43(33):4278–4290.
- Tang CY, Zhao Y, Wang R, Hélix-Nielsen C, Fane AG (2013) Desalination by biomimetic aquaporin membranes: Review of status and prospects. *Desalination* 308:34–40.
- Barboiu M, Gilles A (2013) From natural to bioassisted and biomimetic artificial water channel systems. *Acc Chem Res* 46(12):2814–2823.
- Fei Z, et al. (2005) A synthetic zwitterionic water channel: Characterization in the solid state by X-ray crystallography and NMR spectroscopy. *Angew Chem Int Ed* 44(35):5720–5725.
- Kaucher MS, et al. (2007) Selective transport of water mediated by porous dendritic dipeptides. *J Am Chem Soc* 129(38):11698–11699.
- Le Duc Y, et al. (2011) Imidazole-quartet water and proton dipolar channels. *Angew Chem Int Ed* 50(48):11366–11372.
- Hu X-B, Chen Z, Tang G, Hou J-L, Li Z-T (2012) Single-molecular artificial transmembrane water channels. *J Am Chem Soc* 134(20):8384–8387.
- Zhou X, et al. (2012) Self-assembling subnanometer pores with unusual mass-transport properties. *Nat Commun* 3(7):949.
- Barboiu M, et al. (2014) An artificial primitive mimic of the Gramicidin-A channel. *Nat Commun* 5:4142.
- Illsley N, Verkman AS (1986) Serial permeability barriers to water transport in human placental vesicles. *J Membr Biol* 94(3):267–278.
- Borgnia MJ, Kozono D, Calamita G, Maloney PC, Agre P (1999) Functional reconstitution and characterization of AqpZ, the E-coli water channel protein. *J Mol Biol* 291(5):1169–1179.
- Zeidel ML, Albalak A, Grossman E, Carruthers A (1992) Role of glucose carrier in human erythrocyte water permeability. *Biochemistry* 31(2):589–596.
- Sakai N, Matile S (2013) Synthetic ion channels. *Langmuir* 29(29):9031–9040.
- Chen L, et al. (2013) Chiral selective transmembrane transport of amino acids through artificial channels. *J Am Chem Soc* 135(6):2152–2155.
- Cragg PJ, Sharma K (2012) Pillar[5]arenes: Fascinating cyclophanes with a bright future. *Chem Soc Rev* 41(2):597–607.
- Ogoshi T, Kanai S, Fujinami S, Yamagishi T-a, Nakamoto Y (2008) *para*-Bridged symmetrical pillar[5]arenes: Their Lewis acid catalyzed synthesis and host-guest property. *J Am Chem Soc* 130(15):5022–5023.
- Ogoshi T, et al. (2010) Facile, rapid, and high-yield synthesis of pillar[5]arene from commercially available reagents and its X-ray crystal structure. *J Org Chem* 76(1):328–331.
- Ogoshi T, Hashizume M, Yamagishi T-a, Nakamoto Y (2010) Synthesis, conformational and host-guest properties of water-soluble pillar[5]arene. *Chem Commun* 46(21):3708–3710.
- Gullapalli RR, Mathura R, Dangaria JH, Butler PJ, Tabouillot T (2007) Integrated multimodal microscopy, time-resolved fluorescence, and optical-trap rheometry: Toward single molecule mechanobiology. *J Biomed Opt* 12(1):014012.
- Hoomann T, Jahnke N, Horner A, Keller S, Pohl P (2013) Filter gate closure inhibits ion but not water transport through potassium channels. *Proc Natl Acad Sci USA* 110(26):10842–10847.
- Erbakan M, et al. (2014) Molecular cloning, overexpression and characterization of a novel water channel protein from *Rhodobacter sphaeroides*. *PLoS One* 9(1):e86830.
- Tong J, Canty JT, Briggs MM, McIntosh TJ (2013) The water permeability of lens aquaporin-0 depends on its lipid bilayer environment. *Exp Eye Res* 113:32–40.
- Maffeo C, Bhattacharya S, Yoo J, Wells D, Aksimentiev A (2012) Modeling and simulation of ion channels. *Chem Rev* 112(12):6250–6284.
- Beckstein O, Sansom MSP (2003) Liquid-vapor oscillations of water in hydrophobic nanopores. *Proc Natl Acad Sci USA* 100(12):7063–7068.
- Hummer G, Rasaiah JC, Noworyta JP (2001) Water conduction through the hydrophobic channel of a carbon nanotube. *Nature* 414(6860):188–190.
- Sotomayor M, Schulten K (2004) Molecular dynamics study of gating in the mechanosensitive channel of small conductance MscS. *Biophys J* 87(5):3050–3065.
- Zhu F, Tajkhorshid E, Schulten K (2004) Collective diffusion model for water permeation through microscopic channels. *Phys Rev Lett* 93(22):224501.
- Zhu F, Tajkhorshid E, Schulten K (2002) Pressure-induced water transport in membrane channels studied by molecular dynamics. *Biophys J* 83(1):154–160.
- Kumar M, Habel JEO, Shen Y-x, Meier WP, Walz T (2012) High-density reconstitution of functional water channels into vesicular and planar block copolymer membranes. *J Am Chem Soc* 134(45):18631–18637.
- Dolder M, Engel A, Zulauf M (1996) The micelle to vesicle transition of lipids and detergents in the presence of a membrane protein: Towards a rationale for 2D crystallization. *FEBS Lett* 382(1-2):203–208.
- Gyobu N, et al. (2004) Improved specimen preparation for cryo-electron microscopy using a symmetric carbon sandwich technique. *J Struct Biol* 146(3):325–333.
- Meinild A-K, Klaerke DA, Zeuthen T (1998) Bidirectional water fluxes and specificity for small hydrophilic molecules in aquaporins 0–5. *J Biol Chem* 273(49):32446–32451.
- Zeidel ML, Ambudkar SV, Smith BL, Agre P (1992) Reconstitution of functional water channels in liposomes containing purified red cell CHIP28 protein. *Biochemistry* 31(33):7436–7440.
- Murata K, et al. (2000) Structural determinants of water permeation through aquaporin-1. *Nature* 407(6804):599–605.
- Noy A, et al. (2007) Nanofluidics in carbon nanotubes. *Nano Today* 2(6):22–29.
- Gruner G (2006) Carbon nanotube transistors for biosensing applications. *Anal Bioanal Chem* 384(2):322–335.
- Buzhynskyy N, Sens P, Behar-Cohen F, Scheuring S (2011) Eye lens membrane junctional microdomains: A comparison between healthy and pathological cases. *New J Phys* 13:085016.
- Corless JM, McCaslin DR, Burton LS (1982) Two-dimensional rhodopsin crystals from disk membranes of frog retinal rod outer segments. *Proc Natl Acad Sci USA* 79(4):1116–1120.
- Miller KR, Jacob JS (1983) Two-dimensional crystals formed from photosynthetic reaction centers. *J Cell Biol* 97(4):1266–1270.
- Walz T, et al. (1997) The three-dimensional structure of aquaporin-1. *Nature* 387(6633):624–627.
- Hite RK, Li Z, Walz T (2010) Principles of membrane protein interactions with annular lipids deduced from aquaporin-0 2D crystals. *EMBO J* 29(10):1652–1658.
- Holt JK, Noy A, Huser T, Eaglesham D, Bakajin O (2004) Fabrication of a carbon nanotube-embedded silicon nitride membrane for studies of nanometer-scale mass transport. *Nano Lett* 4(11):2245–2250.
- Ge L, et al. (2012) Vertically-aligned carbon nanotube membranes for hydrogen separation. *RSC Adv* 2(12):5329–5336.
- Mohammad M, Khan MB, Sherazi TA, Anguita J, Adikaari D (2013) Fabrication of vertically aligned CNT composite for membrane applications using chemical vapor deposition through in situ polymerization. *J Nanomater* 2013:713583.
- Baek Y, et al. (2014) High performance and antifouling vertically aligned carbon nanotube membrane for water purification. *J Membr Sci* 460:171–177.
- Xu T, et al. (2011) Subnanometer porous thin films by the co-assembly of nanotube subunits and block copolymers. *ACS Nano* 5(2):1376–1384.